

1 Retrieving Stratospheric Ozone Profiles from OMPS Limb

2 Profiler Measurements

3 Fang Zhu¹, Xiaoping Liu¹, Suwen Li¹, Fuqi Si²

4 ¹Anhui Province Key Laboratory of Pollutant Sensitive Materials and Environmental Remediation, Anhui Province Key
5 Laboratory of Intelligent Computing and Applications, School of Physics and Electrical Information, Huaibei Normal
6 University, Huaibei, 235000, Anhui, China

7 ²Centre of Environmental Optics, Anhui Institute of Optics and Fine Mechanics, Hefei Institutes of Physical Science,
8 Chinese Academy of Sciences, Hefei, Anhui 230031, China

9
10 *Correspondence to:* Fang Zhu (zhufang160@163.com)

11 **Abstract.** This study presents an independent retrieval algorithm combining wavelength pairing and the multiplicative
12 algebraic reconstruction technique (MART) to process Ozone Mapping and Profiler Suite (OMPS) limb observations for
13 vertical ozone profiles. Developed as a complementary dataset for validating operational products, the algorithm is
14 tailored to OMPS/LP's specific characteristics. The retrieval algorithm employs scattered solar radiance measurements
15 from the OMPS limb profiler, focusing on the visible spectral range, normalizes this radiance to that at an upper tangent
16 height, and retrieves ozone concentrations between 12–40 km. Additionally, it enables the identification of
17 cloud-contaminated measurements at specific altitudes within the instrument field of view. A comprehensive error
18 analysis reveals that prior uncertainty contributes ~5% error in the tropical lower stratosphere (based on a +5%
19 perturbation experiment), while a 30% uncertainty in the aerosol extinction coefficient causes ~5% error at 15–25 km.
20 Absorption cross-section uncertainties introduce localized biases of –3% to –5%, and random measurement noise
21 exhibits strong altitude dependence, with values below 10% in the mid-stratosphere and exceeding 20% at high altitudes
22 and in the tropical upper troposphere. OMPS data spanning the entire year of 2021 are processed, and the results are
23 evaluated through comparisons with multiple independent datasets, including NASA official products, passive satellite
24 observations, and in-situ measurements from balloon-borne ozonesondes. At 17–36 km, deviations from OMPS/LP v2.6
25 data are $\leq 5\%$; at 18–35 km, consistency with Microwave Limb Sounder (MLS) v5.0 data ranges from 5–10%; at 20–35
26 km, most deviations from OSIRIS v7.3 data are $\leq 5\%$ (except near 23 km). Comparisons with ozonesonde
27 measurements reveal that differences in the 13–30 km range over northern mid-to-high latitudes are mostly $< 10\%$ (with
28 10–15% differences at 22–25 km in polar regions). Over southern mid-latitudes, the consistency within the same altitude
29 range is 2–10%. Notably, deviations between the retrieved profiles and comparison products increase significantly in
30 low-altitude tropical regions.

31 1 Introduction

32 Stratospheric ozone forms a natural barrier protecting life on Earth by absorbing solar ultraviolet (UV) radiation.
33 Additionally, as a key greenhouse gas, it participates in the absorption and emission of infrared radiation in the
34 stratosphere, playing a crucial role in regulating Earth's energy balance and stabilizing the climate system (Li, F., et al.,
35 2023). Dynamic changes in stratospheric ozone concentrations not only directly reflect the emission fluxes and chemical
36 reaction processes of various atmospheric substances, but also serve as an important indicator for assessing the impact of
37 human activities on the atmospheric environment (Young et al., 2021; Chipperfield and Bekki, 2024). Since the

38 identification of the Antarctic ozone hole in the 1980s, research on the evolution patterns and driving mechanisms of
39 stratospheric ozone concentration has remained a core topic in atmospheric science, attracting global research efforts to
40 continuously explore its variation mechanisms and ecological effects.

41 High-precision retrieval of stratospheric ozone vertical profiles is a core requirement for advancing stratospheric
42 ozone research and establishing long-term essential climate variable datasets (Jia et al., 2015). To this end, multi-platform
43 monitoring technologies—including ground-based, balloon-borne, airborne, and satellite-based instruments—have been
44 widely applied over recent decades. Among these, satellite observations are categorized by detection modes into nadir,
45 occultation, and limb observations. Nadir-viewing instruments, which observe downward, offer excellent horizontal
46 coverage, with typical examples including the Ozone Monitoring Suite–Nadir (OMS-N) aboard Fengyun-3F
47 (NSMC,2025), the Ozone Monitoring Instrument (OMI) aboard Aura(Veefkind et al., 2006), and the Environmental
48 Monitoring Instrument (EMI) onboard the hyperspectral observation satellite GeoFen-5 (Qian et al., 2024). Occultation
49 instruments, which directly view the solar disk, are represented by the Stratospheric Aerosol and Gas Experiment (SAGE
50 III) (Cisewski et al., 2014), Atmospheric Chemistry Experiment (ACE) (Bernath et al., 2005), and Global Ozone
51 Monitoring by Occultation of Stars (GOMOS) (Bertaux et al., 2010), featuring high vertical resolution and good
52 signal-to-noise ratio. Limb scattering/emission observations combine the advantages of the aforementioned two modes,
53 boasting high sensitivity, favorable vertical resolution, and high spatial sampling rates, such as the Microwave Limb
54 Sounder (MLS) (Waters et al., 2006), SCanning Imaging Absorption spectroMeter for Atmospheric CartographY
55 (SCIAMACHY) (Burrows et al., 1995), and Optical Spectrograph and InfraRed Imager System (OSIRIS) (Llewellyn et
56 al., 2004). The Ozone Mapping and Profiler Suite (OMPS), a passive imaging spectrometer employed in this study, is
57 onboard the Suomi-National Polar-orbiting Partnership (SNPP) satellite (Flynn et al. 2014). Its limb profiler (OMPS/LP)
58 enables accurate retrieval of stratospheric ozone vertical profiles via limb observation mode. Since 2012, the NASA team
59 has successively developed and released four versions of the ozone LP retrieval algorithm for OMPS limb observation
60 data (the first version was released with operations (Rault et al,2013), the second version in 2014 (Xu et al.,2014),
61 version 2.5 in 2017 (DeLand et al., 2017), and version 2.6 in 2023(Kramarova, 2023)). The University of Bremen has
62 also applied its self-developed retrieval algorithm to OMPS/LP measurements (Arosio et al., 2018). In addition, another
63 approach to processing OMPS/LP data employs a 2-D geometry retrieval method, as demonstrated in the work conducted
64 at the University of Saskatchewan (Zawada et al., 2018).

65 This study focuses on ozone profile retrieval from OMPS/LP observation data, employing a retrieval algorithm
66 based on wavelength pairing and the multiplicative algebraic reconstruction technique (MART). The algorithm is derived
67 from the OSIRIS ozone profile retrieval scheme developed by the University of Saskatchewan. While the core retrieval
68 methodology of wavelength pairing and MART is well-established in limb sounding, the novelty of this work lies in its
69 tailored adaptation to the OMPS/LP instrument. Given the significant differences between OMPS/LP and OSIRIS in
70 measurement technologies—including spectral resolution, spectral channels, wavelength range, atmospheric sampling,
71 and radiance acquisition—this study has performed targeted optimizations and innovations on the algorithm. These
72 include significant adaptations in radiative transfer model construction, selection of retrieval spectra, and application of
73 atmospheric parameter databases. Furthermore, this study provides an independently developed retrieval pathway for
74 OMPS/LP, offering a complementary source for cross-validation with official products.

75 The study aims to demonstrate the effectiveness of the wavelength pairing and MART algorithm for retrieving
76 OMPS/LP ozone profiles, thereby laying a theoretical and technical foundation for integrating OMPS/LP and OSIRIS
77 data to construct long-term continuous datasets. The structure of this paper is as follows: Section 2 details the
78 characteristics of the OMPS instrument, discussing its observational geometric principles and key issues in L1 data
79 calibration. Section 3 systematically elaborates on the retrieval algorithm, including its core framework, application
80 strategy of cloud filters, and parameter setting methods for the radiative transfer model. Section 4 conducts
81 multi-dimensional validation and statistical analysis of the retrievals in this study, against NASA ozone profile products,

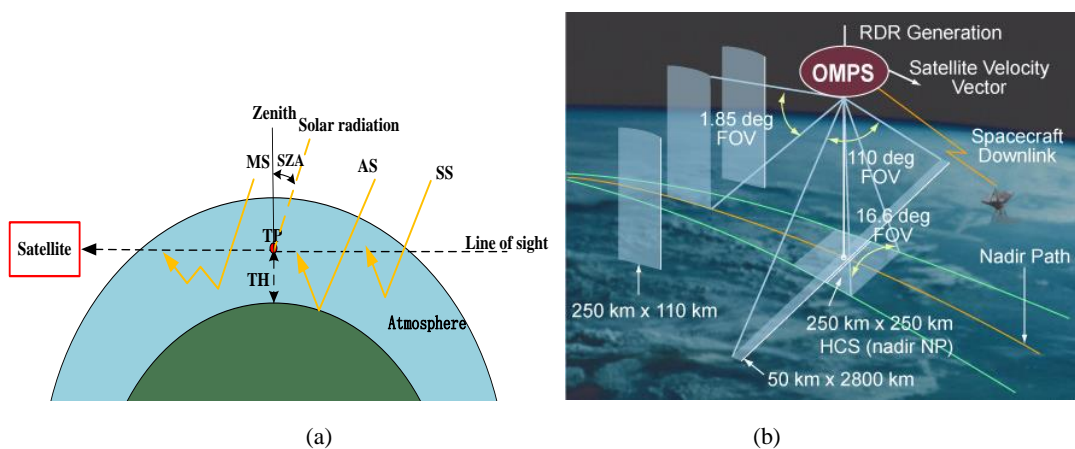
82 MLS, OSIRIS, and ozonesonde datasets. Finally, the main results, key findings are summarized, and potential directions
 83 for future algorithm improvement are outlined in the conclusions.

84 2 OMPS/LP Ozone Retrieval

85 2.1 OMPS/LP instrument

86 The OMPS instrument was successfully launched aboard the SNPP satellite on October 28, 2011 (Zhu et al., 2025).
 87 The satellite operates in a sun-synchronous polar orbit at an average altitude of 833 km with a 13:30 local time ascending
 88 node, commencing routine scientific observations in early 2012 (Kramarova et al., 2022). The OMPS suite integrates
 89 three distinct sensors: the Nadir Mapper (NM), Nadir Profiler (NP), and Limb Profiler (LP) (Flynn et al., 2014). Among
 90 them, OMPS/LP is centrally aimed at retrieving the vertical distribution of ozone in the Earth's middle atmosphere with
 91 high precision, employing a limb observation mode to sound the atmosphere by imaging the edge of the Earth's
 92 atmosphere. During a limb observation, the sensor's line-of-sight passes tangentially through the atmosphere, and the
 93 point along this path with the lowest altitude is termed the tangent point (TP). The vertical distance from this point to the
 94 Earth's geoid is referred to as the tangent height (TH). The fundamental geometry of this observation mode is depicted in
 95 Fig. 1a.

96 The spectral coverage of OMPS/LP ranges from 290 nm to 1000 nm, with spectral resolution varying with
 97 wavelength from 1.5 nm at short wavelengths to 40 nm at the longer-wavelengths (Kramarova et al., 2014). Equipped
 98 with a charge-coupled device (CCD), the instrument can simultaneously observe scattered solar radiation across the full
 99 spectral range at altitudes from 0 to 100 km. Each detector pixel possesses an instantaneous vertical field of view of
 100 approximately 1.5 km. This configuration enables a high-precision vertical sampling of 1 km at the tangent point. (Jaross
 101 et al., 2014). To expand cross-track coverage, OMPS/LP is configured with three observation slits horizontally spaced by
 102 4.25° (approximately 250 km), whose observational geometry and field-of-view characteristics are illustrated in Fig. 1b.
 103 Each slit has a 1.85° vertical field of view (FOV), corresponding to a 110 km vertical observation range at the TP. This
 104 study focuses on measurement data from the central slit, which is aligned with the satellite's ground track. The SNPP
 105 satellite completes 14 orbits daily, with OMPS/LP performing approximately 160–180 measurements per orbit (at a
 106 latitudinal sampling interval of $\sim 1^\circ$). LP can achieve global coverage every 3–4 days (Kramarova et al., 2024).



107
 108
 109 **Figure 1.** (a) Schematic of the satellite limb observation geometry, indicating the key parameters of tangent point (TP) and tangent
 110 height (TH) (SS: single scattering, AS: albedo scattering, MS: multiple scattering, SZA: solar zenith angle) (adapted from Arosio et al.,
 111 2018); (b) Schematic diagram of OMPS observation geometry and field-of-view characteristics (Kramarova et al., 2018).

112 2.2 Key corrections in OMPS/LP L1G v2.6 data

113 Radiometric errors and sensor pointing errors are the two main error sources affecting limb-scattering ozone
114 retrieval accuracy (Kramarova et al., 2024). The OMPS/LP L1G v2.6 dataset incorporates essential corrections to address
115 these issues.

116 Pointing (altitude registration) corrections are applied to mitigate tangent height offsets caused by instrument
117 alignment and thermal effects. Multi-point corrections include static, intra-orbit, and time-dependent adjustments
118 following Moy et al. (2017).

119 Stray light correction is performed using an updated point spread function (PSF) based on pre-launch
120 measurements (Jaross et al., 2014). In version 2.6, the PSF tail intensity in UV and VIS/NIR bands is increased by ~12%
121 to improve high-altitude stray light estimation (Kramarova et al., 2024). An additional factor of 1.5 is applied in VIS/NIR
122 wavelengths to correct for in-band scattering. While thermally induced wavelength shifts have negligible impact on
123 height-normalized radiances in ozone retrieval, we note that residual wavelength-dependent errors could affect
124 cross-section matching in regions of strong ozone absorption.

125 These calibration steps are critical for ensuring the radiometric and geometric accuracy of the radiances used in
126 our retrieval. Further details can be found in the cited references.

127 3 Retrieval method

128 3.1 Retrieval vector

129 The retrieval method for vertical ozone concentration distributions based on OMPS/LP measurements in this study
130 draws on the technical framework developed by Zhu et al.(2021), who derived ozone number density profiles using
131 SCIAMACHY limb scattering measurements in the Chappuis–Wulf band. It shares similar methodological principles
132 with the approaches proposed by Roth et al. (2007) and Degenstein et al. (2009), all of which employ retrieval vectors
133 positively correlated with ozone concentrations for calculations.

134 The first step in the retrieval process involves normalizing the limb radiance at selected wavelengths. This
135 operation entails normalizing the limb radiance at each wavelength to a reference TH, which effectively eliminates
136 interference from the solar Fraunhofer structure, weakens the impact of surface reflection, and simultaneously achieves
137 instrument self-calibration (Jia et al., 2015).

$$138 I_{\text{nor}}(\lambda, H) = I(\lambda, H)/I(\lambda, H_{\text{ref}}) \quad (1)$$

139 where, H denotes the TH, and λ represents the wavelength. $I(\lambda, H_{\text{ref}})$ and $I_{\text{nor}}(\lambda, H)$ refer to the radiance at the
140 reference TH and the normalized radiance, respectively. The reference TH is an upper altitude where ozone sensitivity is
141 low; in this study, it is selected as 40.5 km (i.e., the reference TH above the maximum retrieval altitude). Although
142 radiance normalization cannot completely eliminate the influence of surface reflection or correct spectral errors such as
143 wavelength shifts (which affect the calculation of ozone absorption cross-sections), it significantly reduces the
144 requirements for both absolute radiometric calibration accuracy and modeling accuracy (Flittner et al., 2000). To mitigate
145 the effect of aerosol scattering, the Chappuis triplet vector (CTV) method proposed by Degenstein et al. (2009) and
146 Flittner et al. (2000) is employed for wavelength pairing. In the Chappuis-Wulf band, the CTV is defined as the
147 difference between the logarithmic average of normalized radiances at two weakly ozone-absorbing wavelengths and the
148 logarithm of the normalized radiance at a wavelength near the ozone absorption peak, thereby isolating the ozone

149 absorption signal from common background scattering effects (e.g., aerosol scattering). It is expressed as:

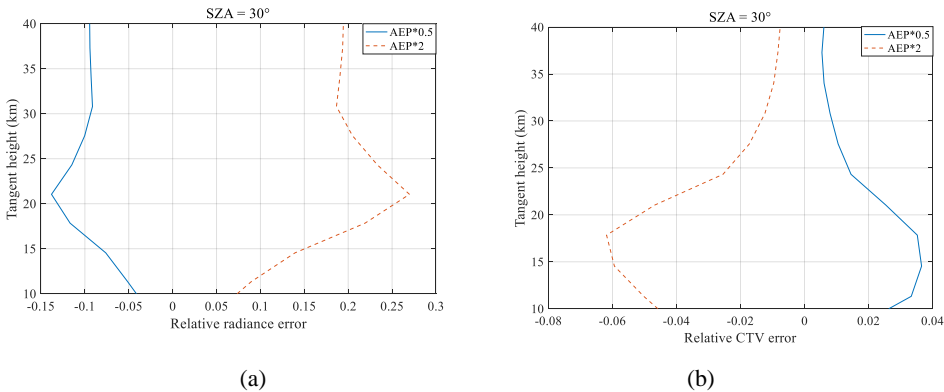
$$150 \quad y_j = \ln \left(\frac{\sqrt{I_{\text{nor}}(\lambda_{\text{ref1},j}) \cdot I_{\text{nor}}(\lambda_{\text{ref2},j})}}{I_{\text{nor}}(\lambda_p,j)} \right) \quad (2)$$

151 where, j denotes the index of the TH measured by the instrument, and y_j represents the retrieval vector after
 152 wavelength pairing at the j^{th} of TH. λ_{ref1} , λ_{ref2} , and λ_p correspond to the weakly ozone-absorbing reference
 153 wavelengths and the strongly absorbing peak wavelength, respectively. In this study, the peak wavelength $\lambda_p=606.3$ nm
 154 adheres to the visible channel configuration employed in the NASA OMPS/LP v2.6 operational algorithm (Kramarova, et
 155 al., 2024), thereby consistency with established OMPS retrieval products. The weakly absorbing reference wavelengths
 156 $\lambda_{\text{ref1}}=512$ nm and $\lambda_{\text{ref2}}=675.5$ nm were optimized according to the selection criteria proposed by Zhu et al. (2021) for
 157 limb scattering ozone retrievals within the Chappuis-Wulf band, which take into account the specific spectral response
 158 and noise characteristics of OMPS/LP. Unlike the NASA algorithm, which uses spectral averages over multiple
 159 wavelengths for its visible triplet (510 nm, 606 nm, 675 nm; Kramarova and DeLand, 2023), the proposed method adopts
 160 individual discrete wavelength channels.

161 The paired measurement vectors maintain high sensitivity to ozone concentration. The CTV is designed to be
 162 positively correlated with ozone concentration (Degenstein et al., 2009). As expected, the CTV values and the retrieved
 163 ozone profiles show consistent vertical and latitudinal variations, with peak altitudes decreasing from the tropics to high
 164 latitudes. In this study, CTV values near zero above 35 km exhibit insufficient sensitivity to ozone, and values above
 165 40 km become negative; therefore, the retrieval is restricted to altitudes below 40 km.

166 Aerosols, as suspended particles capable of absorbing and scattering light, have sources including both natural and
 167 anthropogenic factors. Stratospheric aerosols mainly originate from SO_2 , HCl released by volcanic eruptions, naturally
 168 generated OCS, and pollutants such as SO_2 from industrial emissions (Li, Z., et al., 2023). The presence of aerosols
 169 enhances the intensity of atmospheric scattered light, with the effect being stronger at longer (red) wavelengths than at
 170 shorter (blue) wavelengths due to wavelength-dependent scattering. Based on the SCIATRAN model (radiative
 171 TRANSfer model for SCIAMACHY), this study conducted simulation experiments on aerosol extinction coefficients to
 172 explore their impacts on radiance and CTV.

173 Fig. 2 shows the effects of aerosol extinction profiles with different scaling factors on radiance and CTV. When the
 174 aerosol profile varies within the range of 0.1-10 times the standard value, the radiance profile is positively correlated with
 175 the aerosol extinction coefficient, while CTV decreases as the extinction coefficient increases, with the impact mainly
 176 concentrated below 30 km. For instance, when the aerosol extinction profile doubles, the radiance value at 21 km
 177 increases by 27%, while CTV decreases by only 5%. It indicates that wavelength pairing can weaken the aerosol
 178 scattering effect but cannot completely eliminate it. In addition, the study found that both radiance errors and CTV errors
 179 increase with an increase in SZA.



180
 181
 182 **Figure 2.** Variations in radiance and CTV with aerosol extinction coefficients of different multiples. (a) Relative radiance error; (b)
 183 Relative CTV error.

184 3.2 Multiplicative algebraic relaxation technology

185 Given the nonlinear nature of the retrieval problem, this study employs an iterative method for solution and selects
186 the multiplicative algebraic reconstruction technique (MART) to perform ozone profile retrieval. As an improved
187 algorithm of nonlinear relaxation techniques, MART has a main advantage in that it can utilize multiple sets of
188 measurement vectors to realize the retrieval of atmospheric state parameters at any altitude (Roth et al., 2007). During the
189 iteration process, the update of atmospheric states at each altitude depends on a multiplicative factor, which is obtained
190 by weighted averaging the ratios of all valid observation vectors to simulation vectors. The general formula of the MART
191 algorithm is as follows:

$$192 \quad x_i^{(n+1)} = x_i^{(n)} \sum_j \left(\frac{y_j^{\text{obs}}}{y_j^{\text{mod}}} W_{ji} \right) \quad (3)$$

193 where, $x_i^{(n)}$ denotes the ozone number density at atmospheric height i during the n^{th} iteration; y_j^{obs} and y_j^{mod}
194 represent the observation vector and simulation vector processed via Equations (1) and (2), respectively, where \mathbf{y}^{mod} is
195 generated by the radiative transfer model based on the ozone profile $\mathbf{x}^{(n)}$ obtained from the n^{th} iteration; W_{ji} is the
196 line-of-sight weight factor, indicating the importance of the j^{th} TH or line of sight to the ozone retrieved at altitude i . At
197 each altitude, $\sum_j W_{ji} = 1$. The value of W_{ji} in this study follows the setting in Zhu et al., (2021).

198 3.3 Cloud filter

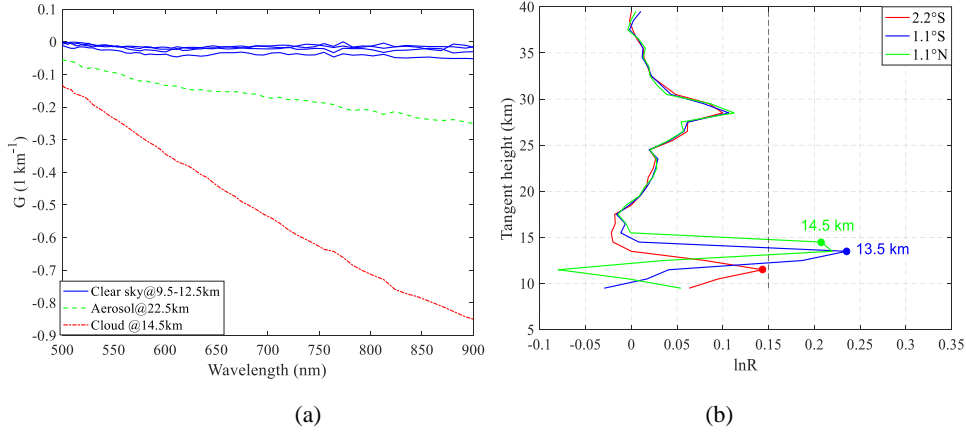
199 A critical step in the OMPS/LP ozone profile retrieval is to define the lower boundary by determining cloud top
200 height. This is accomplished using a cloud detection method, modified from Chen et al. (2016), which leverages the
201 spectral contrast in radiance between red and near-infrared bands. The method quantifies this contrast by computing the
202 change in the vertical radiance gradient between two selected wavelengths. The underlying premise of the gradient-based
203 cloud detection algorithm is that clouds generate a significantly larger radiance gradient compared to aerosols. This
204 gradient is quantitatively defined as the rate of change of radiance with respect to TH:

$$205 \quad \mathbf{G}(\lambda, H) = \partial \ln I(\lambda, H) / \partial H \quad (4)$$

206 As shown in Fig. 3a, the variation characteristics of radiance gradient with wavelength in the 500-900 nm provide a
207 basis for determining cloud top height. In cloud-free conditions, the radiance intensity varies slightly with wavelength;
208 whereas in the presence of clouds, the wavelength dependence of radiance is significantly stronger than that of aerosols.
209 Based on this, in this study, the cloud top height is determined by calculating the spectral gradient difference, with the
210 formula as follows:

$$211 \quad \ln \mathbf{R}(H) = [\mathbf{G}(\lambda_s, H) - \mathbf{G}(\lambda_l, H)] \quad (5)$$

212 where, λ_s and λ_l denote the short wavelength and long wavelength, respectively. In this study, λ_s is set to 674 nm, and
213 λ_l is set to 868 nm. The positive cloud detection threshold for LP data is 1.5, which is also applicable to the detection of
214 polar mesospheric clouds (PMCs). Taking the SNPP satellite orbit 51220 on September 15, 2021 as an example (Fig.3b),
215 the characteristics of $\ln \mathbf{R}$ profiles differ significantly between two cloudy events and one cloud-free event: the
216 maximum value of $\ln \mathbf{R}$ in the cloud-free event is below 1.5, while that in the cloudy events is above this threshold, and
217 the TH corresponding to the maximum $\ln \mathbf{R}$ value is the cloud top height. During the ozone retrieval process, retrieval
218 below the cloud top height is not performed, and the profile in this region remains unchanged.



219
220

221 **Figure 3.** Radiance gradient $G(\lambda, H)$ and gradient difference $\ln R$ during orbit 51220 on September 15, 2021. (a) Radiance gradient
 222 $G(\lambda, H)$ spectrum at 3°N under different atmospheric conditions: clear sky (blue), cloud (red), and aerosol (green); (b) Radiance
 223 gradient difference $\ln R$ derived from OMPS/LP measurements for three equatorial events, showing the cloud detection results. The
 224 black dashed line represents the threshold employed for cloud identification.

225 **3.4 Implementation details**

226 In this study, the SCIATRAN v2.2 toolbox (Rozanov et al., 2017) is employed as the forward modeling to calculate
 227 the simulated radiances required for ozone concentration retrieval. The observed and simulated radiances are processed
 228 through normalization and wavelength pairing to form retrieval vectors, which serve as inputs to the MART algorithm to
 229 drive the iterative update of ozone profiles.

230 The radiative transfer solution in the forward model is based on the discrete ordinate method applied to a spherical
 231 atmosphere with a pseudo-spherical approximation for multiple scattering. The solution incorporates the effects of
 232 multiple scattering and refraction while explicitly omitting polarization. Radiance calculations in the model are focused
 233 solely on ozone, an absorbing gas, with the ozone absorption cross-sections referenced from the research results of
 234 Bogumil et al. (2000). The pressure and temperature profiles used in this study were obtained from the Global Modeling
 235 and Assimilation Office (GMAO) interpolated dataset. These meteorological data are incorporated in the OMPS/LP L1G
 236 dataset provided by NASA (NASA, 2025a). In addition, the model sets the stratospheric background aerosol type as
 237 LOWTRAN (Kneizys, 1988), the boundary layer humidity as 80%, and the boundary layer aerosol type as marine. The
 238 retrieved ozone profiles are reported on the same vertical grid as the OMPS/LP L1G input data, which has a fixed
 239 spacing of 1 km in tangent height. However, this sampling interval does not imply an equivalent effective vertical
 240 resolution. The true vertical resolution is generally coarser than 1 km, particularly in regions of lower measurement
 241 sensitivity. The prior profiles are from SCIATRAN's built-in database. These profiles are provided by McLinden
 242 climatology (C. McLinden, Meteorological Service of Canada, personal communication) and include monthly and
 243 latitude-dependent vertical distributions of volume mixing ratios for O_3 , NO_2 , BrO , and OCIO , as well as pressure and
 244 temperature in the 0 to 100 km altitude range. The volume mixing ratio of ozone can be converted to ozone number
 245 density based on temperature and pressure.

246 **4 Results**

247 This section presents the processing results derived from the full year of 2021 OMPS-LP data. We utilized the L1G
 248 v2.6 dataset (Jaross, 2023), which incorporates enhanced stray light correction and pointing accuracy as detailed in

249 Section 2.2. The analysis is based exclusively on measurements from the instrument's central slit.

250 4.1 Error analysis

251 In the field of error analysis on limb-scattering ozone retrieval, there is a wealth of academic achievements. Zhu et
252 al. (2022) used numerical perturbation to conduct formal error analysis on the retrieval method of the weighted
253 multiplicative algebraic reconstruction technique, accurately quantifying ozone retrieval errors at different altitudes.
254 Arosio et al. (2022) systematically evaluated random errors and systematic errors for stratospheric ozone profile retrieval
255 based on Optimal Estimation (OE) algorithms. These research results provide important references for the error analysis
256 of MART retrieval algorithm, and the error estimation results of this study are consistent with those in Arosio et al. (2022)
257 and Zhu et al. (2022).

258 To ensure data quality, radiance measurements contaminated by clouds were systematically excluded during
259 retrieval. Furthermore, the scene reflectance was determined directly from OMPS/LP radiance measurements at 675 nm,
260 and the corrected THs provided in the NASA LIG data were adopted. Accordingly, the retrieval error budget focuses on
261 four primary sources: prior profiles, aerosols extinction profile, ozone absorption cross-sections, and measurement noise.

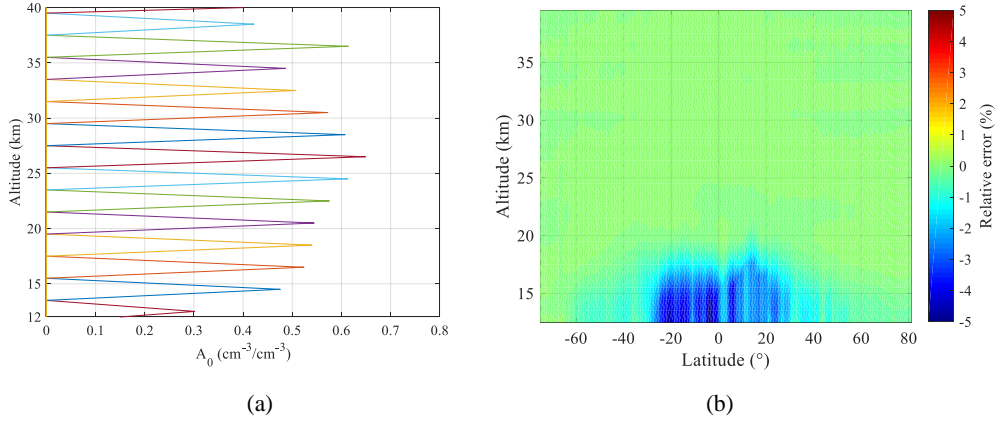
262 The sensitivity of retrieval to the true state and the contribution of prior information can be formally described
263 through the averaging kernel and measurement response (Rodgers, 2000; von Clarmann et al., 2020). However, unlike
264 OE approaches, the MART algorithm used in this study does not produce formal averaging kernels. Therefore, we assess
265 the sensitivity of the retrieval to the prior profile through a perturbation-based approach. In this study, the prior sensitivity
266 analysis matrix \mathbf{A}_0 is used to quantify the sensitivity of retrieval to the prior profile, and its expression is as follows:

$$267 \mathbf{A}_0 = \frac{\partial \hat{\mathbf{x}}}{\partial \mathbf{x}_0} \quad (6)$$

268 where \mathbf{x}_0 and $\hat{\mathbf{x}}$ represent the initial ozone profile and the retrieved ozone profile, respectively. To calculate the column
269 vectors of \mathbf{A}_0 , the ozone concentration at a single altitude was perturbed in \mathbf{x}_0 by 5% and analyzes the corresponding
270 changes in $\hat{\mathbf{x}}$. \mathbf{A}_0 is a dimensionless matrix, whose characteristics can intuitively reflect the impact of changes in the
271 prior profile on the retrievals.

272 Fig. 4a illustrates the distribution of the prior sensitivity analysis matrix (\mathbf{A}_0) column vectors across the 12–40 km
273 altitude range, with each curve plotted at a vertical grid resolution of 2 km. A peak centered near the perturbation altitude
274 indicates that the retrieval at that altitude retains sensitivity to the prior value at the same level. The width of the peak
275 reflects the degree of vertical smoothing inherent in the retrieval. At the lower boundary (below 15 km), the response
276 amplitudes are weak, indicating that perturbations in the prior at these altitudes have limited influence on the retrieved
277 profile. This is consistent with the reduced information content of limb measurements in the upper troposphere and lower
278 stratosphere, where the retrieval is primarily constrained by the measurement geometry and cloud filtering rather than the
279 prior.

280 While Fig. 4a illustrates the pattern of prior influence, it does not quantify the actual retrieval error that would result
281 from an inaccurate prior. To assess this, the entire prior profile was uniformly scaled by +5% at all altitudes, and the
282 relative difference between the perturbed retrieval and the standard retrieval was computed. Fig. 4b shows the relative
283 error induced by a +5% perturbation of the prior profile. Below 20 km, the retrieval shows sensitivity to the a priori, with
284 relative errors -5% in tropical regions. This indicates that a small increase in the prior profile leads to a noticeable
285 underestimation of retrieved ozone concentrations in the tropical lower stratosphere, reflecting the high sensitivity of the
286 retrieval to prior information in this region where measurement information content is low. With increasing altitude, the
287 magnitude of the error progressively decreases. Above 25 km, the error approaches 0% across all latitudes, At high
288 latitudes, the error magnitude remains relatively small at all altitudes, indicating weaker prior dependence compared to
289 tropical and mid-latitude regions.



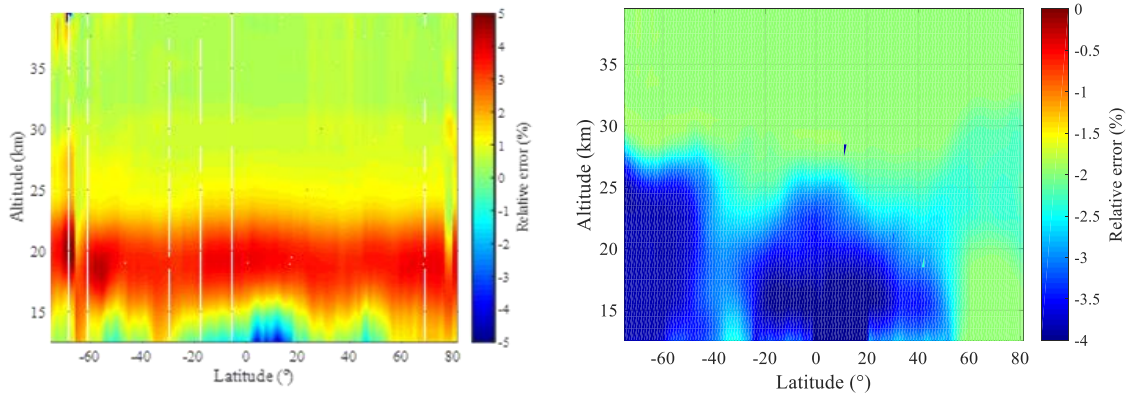
290
291

292 **Figure 4.** Examples of A_0 (plotted every 2 km) and theoretical accuracy of prior profiles. (a) Distribution of A_0 for measurements at
293 2.2 °S; (b) Relative retrieval error resulting from a uniform +5% perturbation of the entire prior profile (orbit 51220 on September 15,
294 2021).

295 The uncertainty of stratospheric aerosol extinction coefficients must be considered in the error budget for ozone
296 profile retrievals. Previous studies have shown that retrieved aerosol extinction profiles have an average upper error
297 bound of approximately 30% in the lower stratosphere (Arosio et al., 2022). To assess the impact of this uncertainty on
298 our ozone retrieval, we perturbed the climatological aerosol extinction profile by uniformly scaling it by +30% at all
299 altitudes and repeated the retrieval. The relative difference between the perturbed retrieval and the standard retrieval was
300 then computed. Fig. 5a depicts the resulting ozone retrieval errors as a function of latitude and altitude. It is evident that
301 retrieval errors induced by variations in aerosol extinction coefficients are predominantly distributed within the 15-25 km
302 altitude range, with a magnitude of approximately 5%, and errors in the southern high latitudes are more pronounced.
303 Within the 25-30 km range, the error is around 2%, while above 30 km, it is less than 1%. Below 15 km, errors vary with
304 latitude, mostly falling within the range of $\pm 2\%$.

305 The temperature dependence of ozone absorption cross-sections has the potential to introduce errors in the
306 retrieved profiles. To assess this effect quantitatively, we followed the approach which applied a uniform +2%
307 perturbations to the ozone absorption cross-sections at all temperatures used in the forward model. This perturbation
308 magnitude represents a typical conservative estimate of cross-section uncertainty in the Chappuis band (Arosio et al.,
309 2022). The retrieval was then repeated using the perturbed cross-sections, and the relative difference relative to the
310 standard retrieval was computed.

311 As shown in Fig. 5b, the resulting retrieval error exhibits a distinct vertical and latitudinal structure. In the tropics,
312 the largest negative deviations (-3% to -5%) appear below 20 km, indicating that retrievals in the tropical lower
313 stratosphere are most sensitive to uncertainties in ozone absorption cross-sections. In the Southern Hemisphere (SH)
314 mid-to-high latitudes, prominent negative deviations (-3% to -4%) are found below 26 km. In the Arctic region, the
315 negative bias below 20 km is relatively smaller, at approximately -2% . Across all latitudinal bands, the error stabilizes
316 near -2% above 25 km. These results confirm that uncertainties in ozone absorption cross-sections introduce systematic
317 biases in lower stratospheric ozone retrievals, especially in the tropics and SH mid-to-high latitudes. Specifically, a
318 positive perturbation in the cross-sections leads to an underestimation of ozone concentrations, as observed in the
319 negative biases in Fig. 5b.



(a) (b)

Figure 5. Distribution of relative errors in ozone retrieval with latitude and altitude, resulting from: (a) a +30% uniform perturbation of the aerosol extinction profile; (b) a +2% uniform perturbation of ozone absorption cross-sections at all temperatures.

To quantify the impact of random measurement noise on retrieval precision, a Monte Carlo simulation was performed using data from OMPS/LP orbit 51220. Sixteen representative latitudes spanning from 80 S to 80 N were selected. For each latitude, Gaussian random noise with a standard deviation of 1% was added independently at each tangent height to the retrieval vector y_j (Eq. 2). This process was repeated 100 times, generating 100 independent noisy realizations per latitude. A full MART retrieval was conducted for each realization, producing an ensemble of 100 retrieved ozone profiles for each latitude. The random uncertainty due to measurement noise was quantified as the standard deviation of the 100 retrieved profiles at each altitude, expressed as a percentage of the average of the unperturbed profiles.

Fig. 6 shows the latitudinal and altitudinal distribution of the resulting random uncertainty. Uncertainty remains low (<10 %) at most latitudes within the 20–33 km mid-stratosphere, reflecting robust and stable retrieval performance. Above 30 km, especially at high latitudes, uncertainty increases sharply to above 20 %, which is mainly attributed to weaker signals in the visible spectral range. In the tropics below 20 km, a region of elevated uncertainty (>15 %) is identified, likely associated with low ozone abundances, strong atmospheric variability, or reduced information content from the measurements.

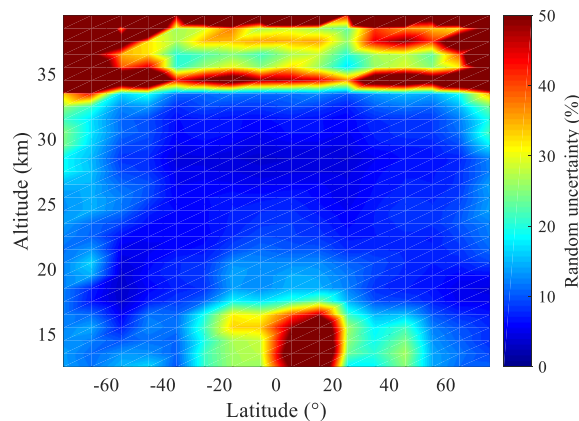


Figure 6. Random uncertainty in retrieved ozone profiles due to measurement noise, quantified as the standard deviation of 100 Monte Carlo realizations with 1% Gaussian noise added to the retrieval vector.

341 4.2 Comparison with NASA OMPS-LP ozone product

342 The OMPS/LP v2.6 ozone profile retrieval algorithm developed by the NASA team is built on wavelength pairing
 343 and an optimal estimation with prior constraints (Kramarova and Deland, 2023). This algorithm operates on combined
 344 UV-Vis measurement data from 12.5 km (or cloud top) to 57.5 km, producing a single ozone profile from each retrieval.
 345 The measurement vectors are obtained via doublet and triplet methods, with specific parameters detailed in Table 1.
 346 During algorithm implementation, the retrieved surface albedo, cloud top height, and corrected tangent height are
 347 incorporated. In the forward model, aerosol extinction coefficients retrieved from OMPS/LP measured data are used.

348 **Table 1.** Parameters used in the OMPS/LP v2.6 ozone algorithm, according to Kramarova and Deland, (2023).

Parameters	Values
Wavelength used in UV (nm)	295, 302, 306, 312, 317, 322, 353
Wavelength used in Vis (nm)	510, 606, 675
Normalization Altitude in UV (km)	60.5 km
Normalization Altitude in Vis (km)	40.5 km

349 Fig. 7 shows a comparison between the retrievals of this study and those of OMPS/LP v2.6, involving
 350 approximately 770,000 profiles. Among them, Fig. 7a presents an example of number density for the annual average
 351 profile, and Fig. 7b shows the relative differences of the annual data. In this study, the relative difference is calculated as
 352 follows:

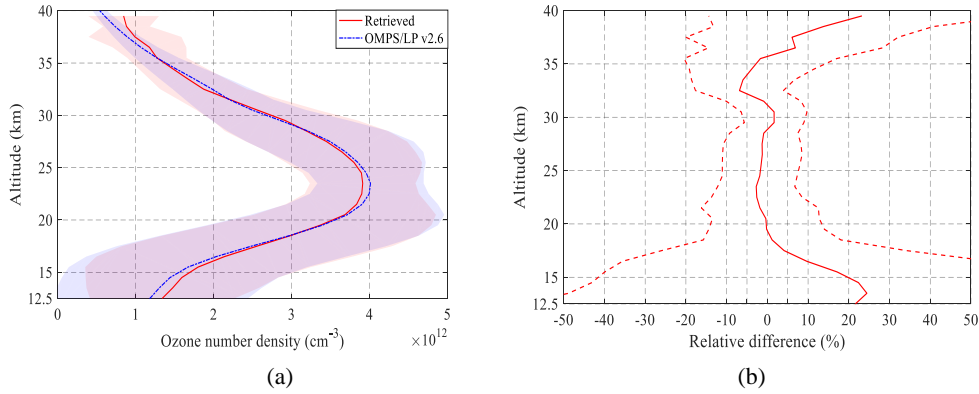
$$353 E_{\text{dif}} = \frac{2 \cdot ([O_3]_{\text{Ret}} - [O_3]_{\text{Ref}})}{([O_3]_{\text{Ret}} + [O_3]_{\text{Ref}})} \times 100\% \quad (7)$$

354 where $[O_3]_{\text{Ret}}$ denotes the ozone profile retrieved in this study, and $[O_3]_{\text{Ref}}$ represents the reference ozone profile
 355 product.

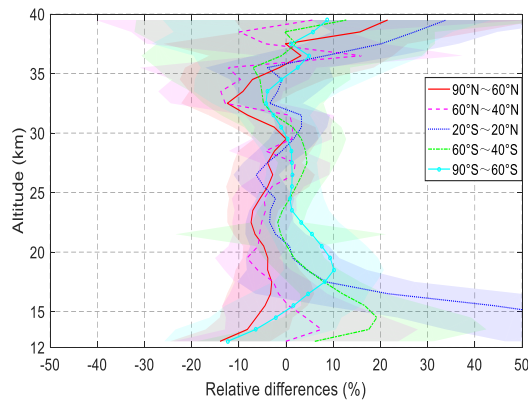
356 As presented in Fig. 7b, the ozone concentrations from our retrieval systematically exceed those of the OMPS/LP
 357 v2.6 product at altitudes below 19 km and above 35 km. The positive deviation increases with decreasing altitude,
 358 reaching a maximum of approximately 10–24% at the upper and lower boundaries of retrieval. The ozone concentration
 359 is slightly lower between 20 and 28 km, with a deviation within 3%. There is an inherent negative deviation of about -6%
 360 around ~ 33 km. Overall, the deviation between 17 and 36 km is confined within 5%.

361 Fig. 8 shows the mean relative differences between the retrievals of this study and OMPS/LP v2.6 in tropical
 362 regions and southern, northern mid-high latitudes. In the tropical regions within the 18–36 km altitude range, the
 363 deviation is within 5%, showing good consistency. At northern mid-high latitudes, the difference between 12 and 32 km
 364 reaches 8%, and the difference above 32 km is as high as 8–13%, with similar deviations in the Arctic region. In the
 365 southern mid-high latitudes, most of the deviations above 18 km are less than 3%, but there is a positive deviation of up
 366 to 19% near 15 km. In the Antarctic region, this positive deviation reaches approximately 10% around 18 km.

367 The two datasets differ significantly in the upper troposphere and lower stratosphere (UTLS) region, especially in
 368 the tropical region, mainly due to the extremely low ozone concentration at this altitude. The large positive deviation at
 369 the upper boundary of retrieval may be caused by the decreased ability of the visible spectrum to retrieve ozone at high
 370 altitudes, while the NASA product uses combined ultraviolet and visible spectrum information for retrieval at this
 371 altitude. Although there are differences between the retrievals of this study and the OMPS/LP v2.6 product in terms of
 372 ozone absorption cross-sections, prior profiles, aerosol settings, retrieval algorithms, and spectra, the overall consistency
 373 is high.



374
 375
 376 **Figure 7.** (a) Annual mean ozone number density profiles from this study and OMPS/LP v2.6, with shaded areas indicating the
 377 standard deviation. (b) The corresponding annual mean relative differences calculated pairwise for each collocated measurement using
 378 Eq. (7), with the standard deviation shown as a dashed line.



379
 380 **Figure 8.** Zonal mean relative differences (this study vs. OMPS/LP v2.6) across five latitudinal bands (60°–90° N, 40°–60° N, 20° S–
 381 20° N, 60°–40° S, 90°–60° S); standard deviations are shown as shaded areas.

382 4.3 Comparison with MLS

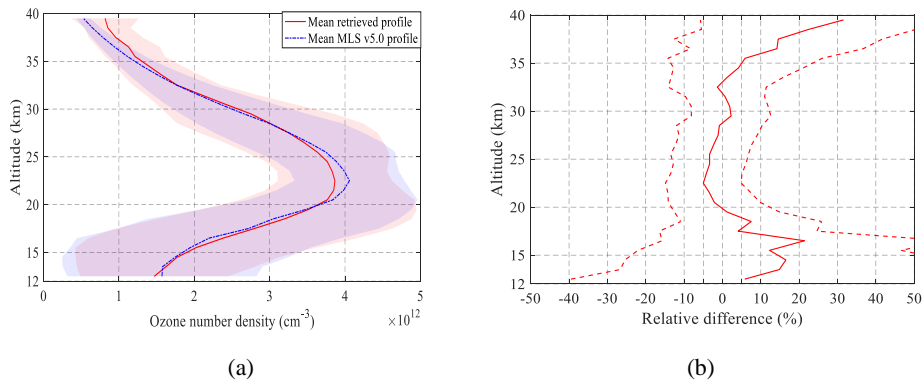
383 The Earth Observing System-Microwave Limb Sounder (EOS-MLS) aboard the Aura satellite was successfully
 384 launched on July 15, 2004 (Waters et al., 2006). The satellite completes about 14 orbits daily, achieving global coverage
 385 between 82° S and 82° N. The MLS obtained vertical ozone profiles from the upper troposphere to the middle atmosphere
 386 using the 240 GHz frequency band by detecting naturally emitted microwave thermal radiation from the Earth's
 387 atmospheric limb measurements. Detailed descriptions can be found by Waters et al. (2006).

388 For validation purposes, this study employs the latest MLS L2 version 5.0 data product (Schwartz et al., 2020), with
 389 data filtering applied in accordance with the protocols recommended by Livesey et al. (2022). To ensure collocation
 390 quality from the dataset, stringent criteria were enforced: we retained only those data pairs where the geographical
 391 separation between the OMPS/LP and MLS footprints was within 1° in both latitude and longitude, and the observation
 392 time difference was less than 6 hours. In cases where multiple MLS profiles corresponded to a single OMPS/LP
 393 measurement, their average was computed and used. For consistent comparison with NASA products and ozonesonde
 394 data, the MLS volume mixing ratio (VMR) and pressure were first transformed to number density and altitude, utilizing
 395 the MLS geopotential height and temperature. These converted profiles were subsequently interpolated onto the regular
 396 altitude grid of the OMPS retrievals using a spline method.

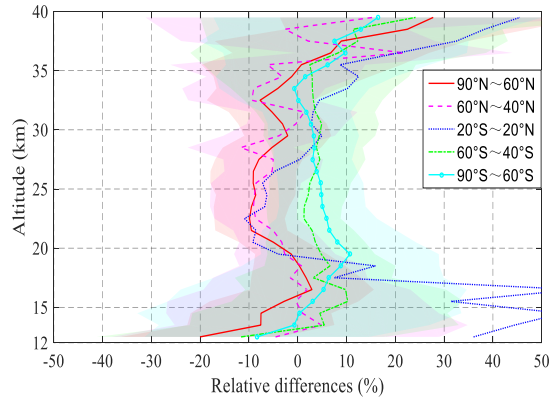
397 Fig. 9 presents the average profiles and relative differences between the retrieval results of this study and MLS v5.0,
 398 involving approximately 93,000 profiles. The results show that compared with MLS v5.0, the ozone concentration

399 retrieved in this study has a relatively large positive deviation of 5–20% below 18 km; the positive deviation above 32
 400 km increases with in altitude; within the 18–35 km height range, the deviation between the two is confined within 5%.

401 Fig. 10 shows the mean relative differences in five latitude zones, with shaded areas indicating the standard
 402 deviations. In terms of data sample size, there are approximately 18,000 profiles in the tropical region, about 20,000 in
 403 the northern high latitudes, and around 15,000 in the southern high latitudes. The analysis results reveal that within the
 404 12–35 km height range, the zonal average relative differences in each latitude zone are basically confined within 10%.
 405 Among them, the northern mid-high latitudes exhibit a stable negative deviation of 5–10% at 20–35 km; the southern
 406 mid-latitudes have a constant positive deviation of 1–5% at 18–36 km, which increases to 3–10% in the polar regions. In
 407 the tropical regions the differences change sign with altitude: the retrieved ozone number density at 19–27 km is 5–10%
 408 lower than that of MLS, while it is 3–10% higher in the 28–36 km range. It is worth noting that below 19 km, the
 409 consistency between the retrieval results of this study and MLS data decreases significantly, with the relative difference
 410 in the tropical region even exceeding 30%, although the absolute difference is relatively small (see Fig. 10a).



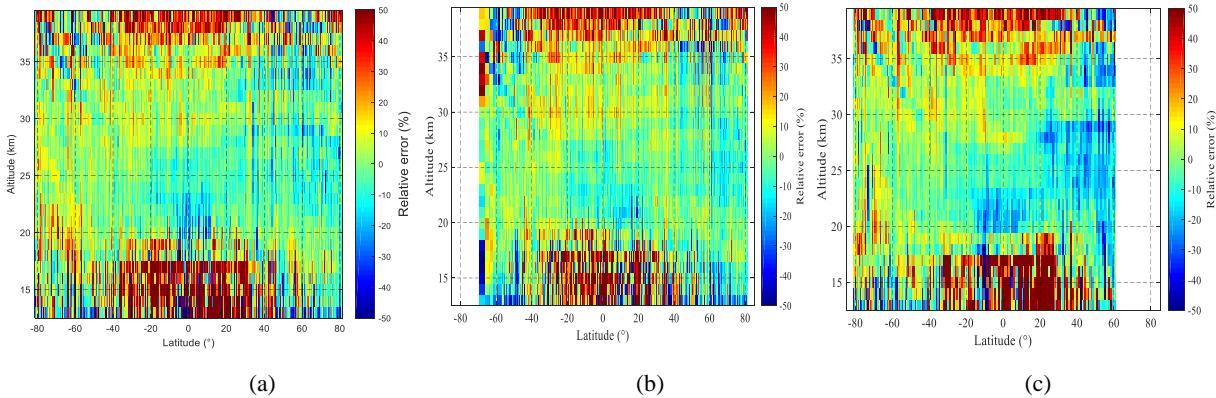
411
 412
 413 **Figure 9.** (a) Annual mean ozone number density profiles from this study and MLS v5.0, accompanied by standard deviations (shaded
 414 areas). (b) The corresponding annual mean relative differences calculated pairwise for each collocated measurement using Eq. (7),
 415 with the standard deviation shown as a dashed line.



416
 417 **Figure 10.** Zonal mean relative differences for (this study vs. MLS v5.0) five latitudinal bands (60°–90° N, 40°–60° N, 20° S–20° N,
 418 60°–40° S, 90°–60° S); standard deviations as shaded areas.

419 Fig. 11 presents the variation of relative differences between retrieval profiles within 1° latitude bins and MLS zonal
 420 averages with altitude, covering three time periods. The full-year 2021 data shown in Fig. 11a indicate that within the
 421 20–35 km altitude range, differences across all latitudes are basically confined within ±10%. The altitude-dependent
 422 behavior of the retrieval biases can be summarized as follows. In the tropical UTLS region, oscillating differences
 423 exceeding 30% are observed, which may be attributed to several factors: the highly dynamic variability of ozone
 424 concentrations, the limited detection sensitivity at the lowest retrieval altitudes, and the influence of cloud filtering.
 425 Furthermore, the inherently low ozone abundance in this region exacerbates retrieval uncertainties. A distinct negative

426 bias in retrieved ozone values is evident at 20–23 km in the tropics, particularly pronounced during winter (Fig. 11c).
 427 Conversely, a positive bias is observed over Antarctica, possibly linked to biases in surface albedo retrieval at high
 428 southern latitudes during polar winter. Above 35 km, the retrievals exhibit a positive bias in the tropics. This altitude
 429 range coincides with the transition zone between ultraviolet and visible spectral windows, where inconsistencies in the
 430 merging of data from these two spectral regions may contribute to the observed discrepancies.



431
 432 (a) (b) (c)
 433 **Figure 11.** Relative differences in ozone number density, averaged over 1° latitude bins and plotted as a function of altitude, for (a) the
 434 entire year of 2021, (b) the boreal summer months (June-August), and (c) December.

435 In summary, the comparative analysis of this study shows that the effectiveness of OMPS retrieval varies across
 436 different regions and altitudes: the accuracy in tropical regions is concentrated in the 20-35 km altitude range; in
 437 mid-latitude regions, good consistency is also observed below 15 km. Nevertheless, in some atmospheric regions and
 438 under different seasonal conditions, the relative deviation may still exceed 10% compared with MLS data.

439 4.4 Comparison with OSIRIS

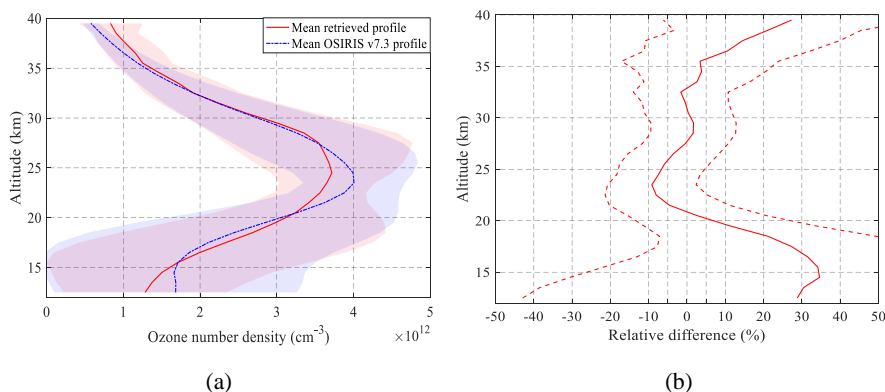
440 In February 2001, the OSIRIS instrument was launched aboard the Odin satellite into a nearly circular
 441 sun-synchronous orbit (Llewellyn et al., 2004). The orbit has an altitude of approximately 600 km, an orbital period of 96
 442 minutes, an inclination of 97.8°, and covers an observational latitude range from 82°S to 82°N. The satellite's ascending
 443 node crosses the equator at approximately 18:00 local time. Detailed descriptions of the instrument can be found by
 444 Llewellyn et al., (2004). Degenstein et al. (2009) used the MART to retrieve ozone profiles in the altitude range from 10
 445 km or cloud top to 60 km, with the retrieval algorithm integrating radiation information from the UV and VIS bands. In
 446 this study, the version of OSIRIS L2 v7.3 data (University of Saskatchewan, 2025) is used for verification.

447 Owing to the sparsity of coincident OSIRIS measurements, a relaxed collocation criterion was adopted. Data pairs
 448 were considered matched if the geographical distance between the instrument footprints was within 2° in latitude and 5°
 449 in longitude, and the time difference was within 24 hours. When multiple OMPS/LP profiles corresponded to a single
 450 OSIRIS observation, their average was used. To unify the data format, the ozone concentration unit (mol/m^3) of OSIRIS
 451 profiles is converted to number density ($/\text{cm}^3$).

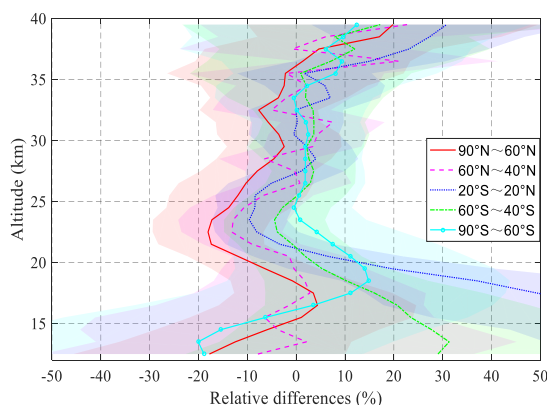
452 Fig. 12 shows the average profiles and relative differences between the retrieval results of this study and OSIRIS
 453 v7.3, involving approximately 44,000 profiles. The results indicate that compared with OSIRIS v7.3, the ozone
 454 concentration retrieved in this study has a relatively large positive deviation of 28-34% below 18 km; above 35 km, the
 455 positive deviation increases with increasing altitude; in the 20-35 km altitude range, except near 23 km, most of the
 456 deviations between the two are confined within 5%.

457 Fig. 13 further compares the mean relative differences of the five latitude zones, with shaded areas indicating the
 458 standard deviations. In terms of data sample size, there are approximately 17,000 profiles in the tropical region, about
 459 10,000 in the northern high latitudes, and around 7,000 in the southern high latitudes. The analysis shows that the

460 northern mid-high latitudes have a significant negative deviation of 5-13% at 21-25 km altitude, which is more prominent
 461 in polar regions; the difference in the southern mid-latitudes at 20-36 km altitude is less than 4%, and the consistency in
 462 the Antarctic region at 23-35 km altitude is better than 2.5%; most of the deviations in the tropical region at 26-36 km
 463 altitude are within 2%. In addition, the differences in the region below 20 km are significant, with the relative difference
 464 in the tropical region exceeding 50% and reaching 30% at 13 km in the southern mid-latitude zone.



465
 466
 467 **Figure 12.** (a) Annual mean ozone number density profiles from this study and OSIRIS v7.3, accompanied by standard deviations
 468 (shaded areas); (b) The corresponding annual mean relative differences calculated pairwise for each collocated measurement using Eq.
 469 (7), accompanied by standard deviations (dashed lines).



470
 471 **Figure 13.** Zonal mean relative differences (this study vs. OSIRIS v7.3) for five latitudinal bands (60°-90° N, 40°-60° N, 20° S-20° N,
 472 60°-40° S, 90°-60° S); standard deviations as shaded areas.

473 4.5 Comparison with ozonesondes

474 To robustly validate the retrieved ozone concentrations at altitudes below 30 km, this study employs a comparative
 475 analysis with ozonesonde measurements. The sonde data were obtained from the World Ozone and Ultraviolet Radiation
 476 Data Centre (WOUDC) and the Southern Hemisphere Additional Ozonesondes (SHADOZ) network (Thompson et al.,
 477 2007). Accounting for the sparse spatial distribution of ozonesonde stations, a relaxed collocation criterion was
 478 implemented: an OMPS/LP measurement was considered a match if it fell within $\pm 5^\circ$ latitude and $\pm 10^\circ$ longitude of a
 479 sonde station and occurred within ± 12 hours of its launch. For each ozonesonde profile, all collocated OMPS/LP
 480 retrievals were averaged to form a single comparative data point.

481 In quantitative comparisons, to align the vertical resolution of ozonesonde data with that of OMPS data, a moving
 482 average filtering method is used for dimensionality reduction of ozonesonde data. The specific procedure begins with
 483 defining the window size of the moving average filter:

484
$$N = \frac{\Delta z_{\text{low}}}{\Delta z_{\text{high}}} \quad (8)$$

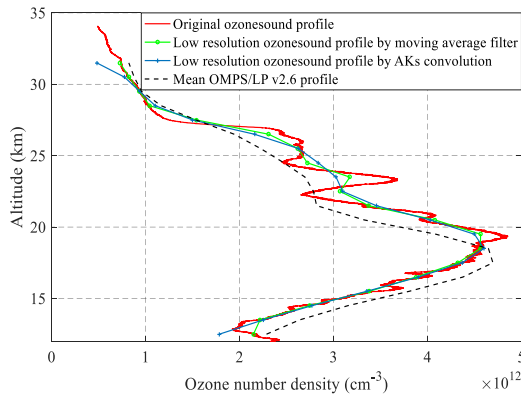
485 where, Δz_{low} and Δz_{high} represent the low vertical resolution of OMPS data and the high vertical resolution of
 486 ozonesonde data, respectively.

487 Filtering is applied to the original ozonesonde data x_{fine} to obtain the dimensionality-reduced data x_{coarse} , which
 488 is expressed as:

489
$$x_{\text{coarse}}(z_k) = \frac{1}{2N+1} \sum_{j=-N}^N x_{\text{fine}}(z_{k+j}) \quad (9)$$

490 where z_k denotes the altitude, and k represents the layer index.

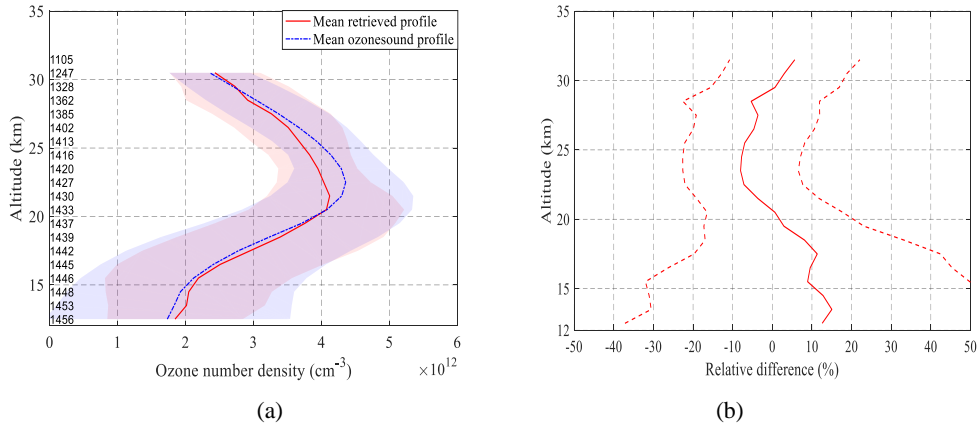
491 In addition, another processing approach involves convolving ozonesonde measurements with the averaging kernels
 492 (AKs) retrieved from OMPS/LP v2.6 (see Arosio et al., (2018) for details). Taking the Alert station (82.5 N, 62.4 W) as
 493 an example, Fig. 14 presents the comparison results between the ozonesonde data and the collocated OMPS average
 494 profile on September 15, 2021. It is found that there are differences in the dimensionality-reduced ozonesonde data
 495 obtained by the two methods. The data curve processed by convolution with averaging kernels is smoother and its shape
 496 is closer to the OMPS product; while the data processed by moving average filter retains more original features with a
 497 sharper curve. After comprehensive consideration, the moving average filter is finally adopted for data processing in this
 498 study.



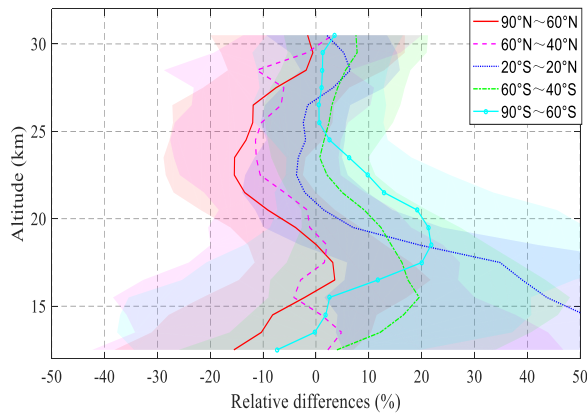
499
 500 **Figure 14.** Ozonesonde data and OMPS collocated average profiles at Alert station on September 15, 2021.

501 Fig. 15 presents the annual average collocated profiles and their relative differences. The left side of the figure
 502 indicates the number of valid collocations at each altitude, with the total sample size amounting to approximately 1460.
 503 This study included data from 41 ozonesonde stations, involving over 1700 individual profiles. A significant positive bias
 504 of 10–15% is observed in the retrievals compared to ozonesonde data below 18 km, while the deviation generally stays
 505 within 10% across the 15–30 km altitude range.

506 Fig. 16 presents the mean relative differences across five latitude zones. The number of available collocations in the
 507 tropical and Antarctic regions is approximately 200 and 75, respectively. Specifically, the tropical region shows good
 508 consistency above 20 km, with most relative differences within $\pm 4\%$ between 20 and 30 km. The southern mid-latitude
 509 region also exhibits high consistency, with positive biases generally less than 5% above 20 km, but a relatively large
 510 positive bias of about 19% near 15 km. In the Antarctic region, the bias is less than 2% above 25 km, while significant
 511 differences occur below 25 km, with a positive bias as high as 21% at 19 km. The northern mid-latitude zone has a bias
 512 of less than 5% below 21 km, but a constant negative bias of 5–11% between 21–28 km, and this negative bias are more
 513 pronounced in the Arctic region.



514
 515
 516 **Figure 15.** (a) Annual mean collocated ozone number density profiles from this study and ozonesonde measurements, accompanied by
 517 standard deviations (shaded areas). (b) Mean relative differences calculated pairwise for each collocated measurement using Eq. (7),
 518 accompanied by standard deviations (dashed lines).



519
 520 **Figure 16.** Zonal mean relative differences (this study vs. ozonesondes) for five latitudinal bands (60°–90° N, 40°–60° N, 20° S–20° N,
 521 60°–40° S, 90°–60° S); standard deviations as shaded areas.

522 **5. Conclusions**

523 This study innovatively applies the ozone profile retrieval method—originally developed at the University of
 524 Saskatchewan for OSIRIS measurements and based on wavelength pairing and the MART—to OMPS/LP observations.
 525 After processing and analyzing the 2021 annual OMPS/LP v2.6 L1G data, observations with the instrument's central slit
 526 and solar zenith angle less than 85° were selected, and ozone profiles between 12.5 and 39.5 km were retrieved. A
 527 comprehensive multi-dimensional validation was conducted.

528 Comparison with the NASA L2 v2.6 official product shows that the overall consistency is good across latitude zones
 529 at 20–36 km, with most differences within ±5%. However, differences near 33 km in the northern mid-latitudes and polar
 530 regions reach up to 10%. Below 20 km, ozone concentrations are relatively high in the Antarctic ozone peak region, with
 531 a pronounced positive bias around 15 km in tropical and southern mid-latitude zones.

532 Validation against MLS v5.0 and OSIRIS v7.3 ozone profiles, as well as ozonesonde data from SHADOZ and
 533 WOUDC, indicates that relative differences with MLS are mostly within ±10% between 13 and 35 km, except for
 534 significant discrepancies in the tropical UTLS region. Compared to OSIRIS v7.3, a negative bias of 13–18% occurs at
 535 20–25 km in northern mid-high latitudes, while positive biases reach 18% at 18 km over Antarctic and exceed 20% at 15

536 km in southern mid-latitudes, with more pronounced deviations in the tropics. Relative to ozonesonde data, differences in
537 tropical and southern mid-latitude regions at 20-30 km remain within $\pm 4\%$, whereas differences of 11-15% are observed
538 at 20-25 km in northern mid-high latitudes. Consistency is good below 20 km in northern mid-latitudes, but positive
539 biases reach 21% at 18 km over Antarctica and 19% at 15 km in southern mid-latitudes.

540 Overall, compared with the reference products, the retrieved ozone concentrations in this study exhibit biases mostly
541 within 5% between 25 and 35 km. A negative bias of 5-10% is observed at 20-25 km in northern mid-high latitudes,
542 particularly in the Arctic. Retrieved values are about 10% higher at the altitude of the Antarctic ozone concentration peak,
543 10–15% higher at 15 km in southern mid-latitudes, and over 30% higher below 20 km in the tropics.

544 The identified biases mainly originate from three factors. Below 20 km, cloud effects remain non-negligible. Even
545 after excluding cloud-affected radiances, retrievals of lower-altitude ozone profiles are still constrained by the initial
546 profile, as no iterative update is applied below the detected cloud top height. Consequently, ozone abundances above
547 cloud tops are overestimated by more than 25%. These discrepancies are further exacerbated by low ozone abundance,
548 strong dynamical variability in the tropics, and the reduced sensitivity of limb retrievals at lower altitudes, while
549 inconsistencies between the background aerosols used in retrievals and real atmospheric conditions also contribute. The
550 overestimation of ozone abundances above 35 km across all latitudes results from the limited sensitivity of the visible
551 spectrum for high-altitude ozone retrievals, in contrast to the operational product that employs combined ultraviolet and
552 visible spectral information.

553 Based on these findings, several priorities for follow-up research are identified. First, integrating operational aerosol
554 extinction products from NASA will be essential to replace the current climatological approach and reduce systematic
555 biases in the UTLS region. Second, including ultraviolet channels will improve retrieval accuracy above 35 km, where
556 visible-only measurements have low sensitivity. Third, refining cloud filtering will better constrain lower altitude
557 retrievals. Finally, the consistent retrieval core shared with OSIRIS lays a solid technical foundation for constructing
558 long-term, coherent stratospheric ozone records, thereby minimizing discrepancies in multi-satellite data merging and
559 supporting climate studies that require stable, multi-decadal observational records.

560 **Data availability**

561 Ancillary information and v2.6 L1G OMPS/LP data were downloaded from <https://disc.gsfc.nasa.gov/datasets>
562 (NASA, 2025a), where L2 data are also available. For the validation sections, MLS L2 data were also taken from <https://disc.gsfc.nasa.gov/datasets>
563 (Schwartz, et al., 2020). OSIRIS v7.3 data were taken from <https://research-groups.usask.ca/osiris/data-products.php> (University of Saskatchewan, 2025). WOUDC data were
564 downloaded on 10 April 2025 from <https://woudc.org/data/explore.php>. A list of all contributors is available on the
565 following website: <https://woudc.org/contributors/>. SHADOZ data were downloaded on 21 April 2025 from
566 <https://tropo.gsfc.nasa.gov/shadoz/Archive.html> (NASA, 2025b).

568 **Author contributions**

569 FZ designed the retrieval algorithm to OMPS/LP observations, processed the data set, performed the validation of
570 the results and wrote the manuscript. FZ and SWL proposed the research and lead the project, analyzed the results and
571 contributed to the writing of the manuscript and the scientific outcomes. XPL contributed the algorithm for cloud filtering,
572 and reviewed the paper. FQS supervised and guided the retrieval process and reviewed the paper.

573 **Competing interests**

574 The authors declare that they have no conflict of interest.

575 **Acknowledgements**

576 This work was supported by the National Science Foundations of China (Grant No. 41875040), and partially funded
577 by the Excellent Research and Innovation Team of Anhui Provincial Department of Education (2023AH010043)

578 We would like to express our sincere gratitude to the NASA OMPS SIPS team for providing data support. We are
579 also thankful to the SCIATRAN radiative transfer model development team.

580 **References**

- 581 Arosio, C., Rozanov, A., Malinina, E., Eichmann, K., von Clarmann, T., and Burrows, J. P.: Retrieval of ozone profiles
582 from OMPS limb scattering observations, *Atmos. Meas. Tech.*, 11, 2135–2149,
583 <https://doi.org/10.5194/amt-11-2135-2018>, 2018.
- 584 Arosio, C., Rozanov, A., Gorshelev, V., Laeng, A., and Burrows, J. P.: Assessment of the error budget for stratospheric
585 ozone profiles retrieved from OMPS limb scatter measurements, *Atmos. Meas. Tech.*, 15, 5949–5967,
586 <https://doi.org/10.5194/amt-15-5949-2022>, 2022.
- 587 Bernath, P. F., McElroy, C. T., Abrams, M. C., Boone, C. D., Butler, M., Camy-Peyret, C., Carleer, M., Clerbaux, C.,
588 Coheur, P. F., Colin, R., DeCola, P., De Mazière, M., Drummond, J. R., Dufour, D., Evans, W. F. J., Fast, H., Fussen,
589 D., Gilbert, K., Jennings, D. E., Llewellyn, E. J., Lowe, R. P., Mahieu, E., McConnell, J. C., McHugh, M., McLeod, S.
590 D., Michaud, R., Midwinter, C., Nassar, R., Nichitiu, F., Nowlan, C., Rinsland, C. P., Rochon, Y. J., Rowlands, N.,
591 Semeniuk, K., Simon, P., Skelton, R., Sloan, J. J., Soucy, M.-A., Strong, K., Tremblay, P., Turnbull, D., Walker, K. A.,
592 Walkty, I., Wardle, D. A., Wehrle, V., Zander, R., and Zou, J.: Atmospheric Chemistry Experiment (ACE): Mission
593 overview, *Geophysical research letters*, 32, L15S01, <https://doi.org/10.1029/2005GL022386>. 2005.
- 594 Bertaux, J. L., Kyrola, E., Fussen, D., Hauchecorne, A., Dalaudier, F., Sofieva, V., Tamminen, J., Vanhellemont, F.,
595 Fanton d'Andon, O., Barrot, G., Mangin, A., Blanot, L., Lebrun, J. C., Perot, K., Fehr, T., Saavedra, L., Leppelmeier,
596 G. W., and Fraisse, R.: Global ozone monitoring by occultation of stars: an overview of GOMOS measurements on
597 ENVISAT, *Atmos. Chem. Phys.*, 10, 12091–12148, <http://doi.org/10.5194/acp-10-12091-2010>, 2010.
- 598 Bogumil, K., Orphal, J., and Burrows, J. P.: Temperature dependent absorption cross sections of O₃, NO₂, and other
599 atmospheric trace gases measured with the SCIAMACHY spectrometer, in: *Proceedings of the*
600 *ERS-Envisat-Symposium*, Goteborg, Sweden, 2000.
- 601 Burrows, J., Hölzle, E., Goede, A., Visser, H., and Fricke, W.: SCIAMACHY–Scanning imaging absorption spectrometer
602 for atmospheric chartography, *Acta Astronautica*, 35, 445–451, [https://doi.org/10.1016/0094-5765\(94\)00278-T](https://doi.org/10.1016/0094-5765(94)00278-T), 1995.
- 603 Cisewski, M., Zawodny, J., Gasbarre, J., Eckman, R., Topiwala, N., Rodriguez-Alvarez, O., Cheek, D., Hall S.: The
604 Stratospheric Aerosol and Gas Experiment (SAGE III) on the International Space Station (ISS) Mission, in:
605 *Proceedings 9241, Sensors, Systems, and Next-Generation Satellites XVIII*, SPIE Remote Sensing, Amsterdam,
606 Netherlands, <https://doi.org/10.1117/12.2073131>, 2014.
- 607 Chen, Z., DeLand, M., and Bhartia, P. K.: A new algorithm for detecting cloud height using OMPS/LP measurements,

608 Atmos. Meas. Tech., 9, 1239–1246, <https://doi.org/10.5194/amt-9-1239-2016>, 2016.

609 Chipperfield, M. P. and Bekki, S.: Opinion: Stratospheric ozone–depletion, recovery and new challenges, *Atmos. Chem.*
610 *Phys.*, 24, 2783–2802, <https://doi.org/10.5194/acp-24-2783-2024>, 2024.

611 Degenstein, D. A., Bourassa, A. E., Roth, C. Z., and Llewellyn, E. J.: Limb scatter ozone retrieval from 10 to 60 km
612 using a multiplicative algebraic reconstruction technique, *Atmos. Chem. Phys.*, 9, 6521–6529,
613 <https://doi.org/10.5194/acp-9-6521-2009>, 2009.

614 DeLand, M., Bhartia, P., Xu, P., Kramarova, N., and Zhu, T.: OMPS Limb Profiler Ozone Product O₃: Version 2.5 Data
615 Release Notes, 2017.

616 Flittner, D. E., Bhartia, P. K., and Herman, B. M.: O₃ Profiles Retrieved from Limb Scatter Measurements: Theory,
617 *Geophysical research letters*, 27(17), 2601–2604, <https://doi.org/10.1029/1999GL011343>, 2000.

618 Flynn, L., Long, C., Wu, X., Evans, R., Beck, C., Petropavlovskikh, I., McConville, G., Yu, W., Zhang, Z., Niu, J., Beach,
619 E., Hao, Y., Pan, C., Sen, B., Novicki, M., Zhou, S., and Seftor, C.: Performance of the ozone mapping and profiler
620 suite (OMPS) products, *J. Geophys. Res.-Atmos.*, 119, 6181–6195, <https://doi.org/10.1002/2013JD020467>, 2014.

621 Jia, J., Rozanov, A., Ladstätter-Weissenmayer, A., and Burrows, J. P.: Global validation of SCIAMACHY limb ozone data
622 (versions 2.9 and 3.0, IUP Bremen) using ozonesonde measurements, *Atmos. Meas. Tech.*, 8, 3369–3383,
623 <https://doi.org/10.5194/amt-8-3369-2015>, 2015.

624 Jaross, G., Bhartia, P. K., Chen, G., Kowitz, M., Haken, M., Chen, Z., Xu, P., Warner, J., Kelly, T.: OMPS Limb Profiler
625 instrument performance assessment, *J. Geophys. Res.-Atmos.*, 119, 4399–4412, <https://doi.org/10.1002/2013JD020482>,
626 2014

627 Jaross, G.: OMPS-NPP L1G LP Radiance EV Wavelength-Altitude Grid swath orbital 3slit V2.6, Greenbelt, MD, USA,
628 Goddard Earth Sciences Data and Information Services Center (GES DISC), Accessed: February 10, 2024,
629 <https://doi.org/10.5067/YVE3FSNJ59RQ>, 2023.

630 Kneizys, F. X.: Users Guide to LOWTRAN 7[M]. Air Force Geophysics Laboratory, 1988.

631 Kramarova, N. A., Nash, E. R., Newman, P. A., Bhartia, P. K., McPeters, R. D., Rault, D. F., Seftor, C. J., Xu, P. Q., and
632 Labow, G. J.: Measuring the Antarctic ozone hole with the new Ozone Mapping and Profiler Suite (OMPS), *Atmos.*
633 *Chem. Phys.*, 14, 2353–2361, <https://doi.org/10.5194/acp-14-2353-2014>, 2014.

634 Kramarova, N. A., Pawan K. Bhartia, Glen Jaross, Leslie Moy, Philippe Xu, Zhong Chen, Matthew DeLand, Lucien
635 Froidevaux, Nathaniel Livesey, Douglas Degenstein, Adam Bourassa, Kaley A. Walker, and Patrick Sheese. Validation
636 of ozone profile retrievals derived from the OMPS LP version 2.5 algorithm against correlative satellite measurements.
637 *Atmos. Meas. Tech.*, 11, 2837–2861, <https://doi.org/10.5194/amt-11-2837-2018>, 2018.

638 Kramarova, N. A., Xu, P., Mok, J., Bhartia, P. K., Jaross, G., Moy, L., Weaver, C., Frith, S., Ziemke, J., Chen, Z., Kahn,
639 D., Nyaku, E., Li, J., Davis, S., and Jia, Y.: Ten Year Ozone Profile Record From Suomi NPP OMPS Limb Profiler,
640 National Oceanic and Atmospheric Administration Washington D.C., District of Columbia, United States, Technical
641 Review NASA Peer Committee December 21, 2022.

642 Kramarova, N. A.: OMPS-NPP L2 LP Ozone (O₃) Vertical Profile swath daily Center slit V2.6, Greenbelt, MD, USA,
643 Goddard Earth Sciences Data and Information Services Center (GES DISC), Accessed: November, 2023,
644 [10.5067/8MO7DEDYTBH7](https://doi.org/10.5067/8MO7DEDYTBH7), 2023.

645 Kramarova, N. A., and DeLand, M.: OMPS Limb Profiler Ozone Product O₃: Version 2.6 Data Release Notes, 36pp,
646 2023.

647 Kramarova, N.A., Xu, P., Mok, J., Bhartia, P. K., Jaross, G., Moy, L., Chen, Z., Frith, S., DeLand, M., Kahn, D., Labow,
648 G., Li, J., Nyaku, E., Weaver, C., Ziemke, J., Davis, S., and Jia, Y.: Decade-long Ozone Profile Record from Suomi
649 NPP OMPS Limb Profiler: Assessment of Version 2.6 Data, *Earth and Space Science*, 11, e2024EA003707,
650 <https://doi.org/10.1029/2024EA003707>, 2024.

651 Li, F., Newman, P. A., and Waugh, D. W.: Impacts of stratospheric ozone recovery on southern ocean temperature and

652 heat budget, *Geophysical Research Letters*, 50(18), e2023GL103951, <https://doi.org/10.1029/2023GL103951>, 2023.

653 Li, Z., Bi, J., Hu, Z., Ma, J., Li, B.: Regional transportation and influence of atmospheric aerosols triggered by Tonga
654 volcanic eruption, *Environmental Pollution*, 325, 121429, <https://doi.org/10.1016/j.envpol.2023.121429>, 2023.

655 Livesey, N. J., Read, W. G., Wagner, P. A., Froidevaux, L., Santee, M. L., Schwartz, M. J., Lambert, A., Millán Valle, L.
656 F., Pumphrey, H. C., Manney, G. L., Fuller, R. A., Jarnot, R. F., Knosp, B. W., and Lay, R. R.: Version 5.0x Level 2 and
657 3 data quality and description document, available at: https://mls.jpl.nasa.gov/data/v5-0_data_quality_document.pdf
658 (last access: June 10, 2025), 2022.

659 Llewellyn, E. J., Lloyd, N. D., Degenstein, D. A., Gattinger, R. L., Petelina, S. V., Bourassa, A. E., Wiensz, J. T., Ivanov,
660 E. V., McDade, I. C., Solheim, B. H., McConnell, J. C., Haley, C. S., von Savigny, C., Sioris, C. E., McLinden, C. A.,
661 Griffioen, E., Kaminski, J., Evans, W. F. J., Puckrin, E., Strong, K., Wehrle, V., Hum, R. H., Kendall, D. J. W.,
662 Matsushita, J., Murtagh, D. P., Brohede, S., Stegman, J., Witt, G., Barnes, G., Payne, W. F., Piché L., Smith, K.,
663 Warshaw, G., Deslauniers, D.-L., Marchand, P., Richardson, E. H., King, R. A., Wevers, I., McCreath, W., Kyrö ä E.,
664 Oikarinen, L., Leppelmeier, G. W., Auvinen, H., Mégie, G., Hauchecorne, A., Lefèvre, F., de La Nöe, J., Ricaud, P.,
665 Frisk, U., Sjöberg, F., von Schöle, F., and Nordh, L.: The OSIRIS Instrument on the Odin Spacecraft, *Canadian*
666 *Journal of Physics*, 82(6), 411-422, <https://doi.org/10.1139/p04-005>, 2004.

667 Moy, L., Bhartia, P. K., Jaross, G., Loughman, R., Kramarova, N., Chen, Z., Taha, G., Chen, G., and Xu, P.: Altitude
668 registration of limb-scattered radiation, *Atmos. Meas. Tech.*, 10, 167–178, <https://doi.org/10.5194/amt-10-167-2017>,
669 2017.

670 NASA: OMPS data, available at: <https://disc.gsfc.nasa.gov/datasets>, last access: February 2025a.

671 NASA: SHADOZ data, available at: <https://tropo.gsfc.nasa.gov/shadoz/Archive.html>, last access: March 2025b.

672 Qian, Y. Y., Luo, Y. H., Zhou, H. J., Yang, T. P., Xi, L., and Si, F. Q.: First Retrieval of Total Ozone Columns from EMI-2
673 Using the DOAS Method, *Remote Sensing*, 16(5): 1234-1245, <https://doi.org/10.3390/rs15061665>, 2024.

674 Rault, D. F. and Loughman, R. P.: The OMPS Limb Profiler Environmental Data Record Algorithm Theoretical Basis
675 Document and Expected Performance, *Ieee Transactions on Geoscience and Remote Sensing*, 51(5): 2505-2527,
676 <https://doi.org/10.1109/TGRS.2012.2213093>, 2013.

677 Rodgers, C. D.: *Inverse methods for atmospheric sounding: theory and practice*. Vol. 2. World scientific, 2000.

678 Roth, C. Z., Degenstein, D. A., Bourassa, A. E., and Llewellyn, E. J.: The retrieval of vertical profiles of the ozone
679 number density using Chappuis band absorption information and a multiplicative algebraic reconstruction technique,
680 *Canadian Journal of Physics*, 85(11), 1225-1243, <https://doi.org/10.1139/p07-130>, 2007.

681 Rozanov, V. V., Dinter, T., Rozanov, A. V., Wolanin, A., Bracher, A., and Burrows J.P.: Radiative transfer modeling
682 through terrestrial atmosphere and ocean accounting for inelastic processes: Software package SCIATRAN. *Journal of*
683 *Quantitative Spectroscopy & Radiative Transfer*, 194, 65-85, <https://doi.org/10.1016/j.jqsrt.2017.03.009>, 2017.

684 Schwartz, M., Froidevaux, L., Livesey, N., and Read, W.: MLS/Aura Level 2 Ozone (O3) Mixing Ratio V005, Greenbelt,
685 MD, USA, Goddard Earth Sciences Data and Information Services Center (GES DISC), Accessed: June 10, 2025,
686 <https://doi.org/10.5067/Aura/MLS/DATA2516>, 2020.

687 Thompson, A. M., Witte, J. C., Smit, H. G., Oltmans, S. J., Johnson, B. J., Kirchhoff, V. W., and Schmidlin, F. J.: Southern
688 Hemisphere Additional Ozonesondes (SHADOZ) 1998–2004 tropical ozone climatology: 3. Instrumentation,
689 station-to-station variability, and evaluation with simulated flight profiles, *J. Geophys. Res.-Atmos.*, 112,
690 <https://doi.org/10.1029/2005JD007042>, 2007.

691 University of Saskatchewan: OSIRIS data. available at: <https://research-groups.usask.ca/osiris/data-products.php>, last
692 access: July 25, 2025.

693 Veefkind, J. P., de Haan, J. R., Brinksma, E. J., Kroon, M., and Levelt, P. F.: Total ozone from the Ozone Monitoring
694 Instrument (OMI) using the DOAS technique, *Ieee Transactions on Geoscience and Remote Sensing*, 44(5):
695 1239-1244, <https://doi.org/10.1109/TGRS.2006.871204>, 2006.

696 von Clarmann, T., Degenstein, D. A., Livesey, N. J., Bender, S., Braverman, A., Butz, A., Compernelle, S., Damadeo, R.,
697 Dueck, S., Eriksson, P., et al.: Overview: Estimating and reporting uncertainties in remotely sensed atmospheric
698 composition and temperature, *Atmospheric Measurement Techniques*, 13(8), 4393-4436, 2020.

699 Waters, J.W., Froidevaux, L., Harwood, R. S., Jarnot, R. F., Pickett, H. M., and Read, W. G.: The Earth Observing System
700 Microwave Limb Sounder (EOS MLS) on the Aura satellite, *Ieee Transactions on Geoscience and Remote Sensing*,
701 44(5), 1075-1092, <https://doi.org/10.1109/TGRS.2006.873771>, 2006.

702 Xu, P. Q., Bhartia, P. K., Jaross, G. R., DeLand, M. T., Larsen, J. C., Fleig, A., Kahn, D., Zhu, T., Chen, Z., Gorkavyi, N.,
703 Warner, J., Linda, M., Chen, H. G., Kowitt, M., Haken, M., and Hall, P.: Release 2 data products from the Ozone
704 Mapping and Profiling Suite (OMPS) Limb Profiler, *Proc. SPIE 9242, Remote Sensing of Clouds and the Atmosphere*
705 *XIX, and Optics in Atmospheric Propagation and Adaptive Systems XVII*, 92420K (17 October 2014),
706 <https://doi.org/10.1117/12.2067320>, 2014.

707 Young, P. J., Harper, A. B., Huntingford, C., Paul, N. D., Morgenstern, O., Newman, P. A., Oman, L. D., Madronich, S.,
708 and Garcia, R. R.: The Montreal Protocol protects the terrestrial carbon sink, *Nature* 596, 384–388,
709 <https://doi.org/10.1038/s41586-021-03737-3>, 2021.

710 Zawada, D. J., Rieger, L. A., Bourassa, A. E., and Degenstein, D. A.: Tomographic retrievals of ozone with the OMPS
711 Limb Profiler: algorithm description and preliminary results, *Atmos. Meas. Tech.*, 11, 2375–2393,
712 <https://doi.org/10.5194/amt-11-2375-2018>, 2018.

713 Zhu, F., Li, S.W., Yang, T. P., and Si, F. Q.: Research on Inversion and Application of Ozone Profile Based on OMPS
714 Limb Scattering Observation, *Acta Optica Sinica*, 45(6), 82-92, <https://doi.org/10.3788/AOS202141.0401005>, 2025.

715 Zhu, F., Si, F. Q., Zhan, K., Dou, K., and Zhou, H. J.: Inversion of Ozone Profile of Limb Radiation in Chappuis-Wulf
716 Band. *Acta Optica Sinica*, 41(4), 39-48, <https://doi.org/10.3788/AOS241244>, 2021.

717 Zhu F., Si, F. Q., Zhou, H. J., Dou, K., Zhao, M. J., and Zhang, Q.: Sensitivity Analysis of Ozone Profiles Retrieved from
718 SCIAMACHY Limb Radiance Based on the Weighted Multiplicative Algebraic Reconstruction Technique, *Remote*
719 *Sensing*, 14(16), 3954, <https://doi.org/10.3390/rs14163954>, 2022.

720
721
722
723
724
725
726
727